The Astrophysical Journal, 829:50 (16pp), 2016 September 20 doi:10.3847/0004-637X/829/1/50

TESTING LSST DITHER STRATEGIES FOR SURVEY UNIFORMITY AND LARGE-SCALE STRUCTURE SYSTEMATICS

Humna Awan[1], Eric Gawiser[1], Peter Kurczynski[1], R. Lynne Jones[2], Hu Zhan[3], Nelson D. Padilla[4], Alejandra M. Muñoz Arancibia[4,5], Alvaro Orsi[6], Sofía A. Cora[7,8,9], and Peter Yoachim[2]
[1] Department of Physics & Astronomy, Rutgers University, 136 Frelinghuysen Rd., Piscataway, NJ 08554, USA; awan@physics.rutgers.edu
[2] Department of Astronomy, University of Washington, 3910 15th Ave NE, Seattle, WA 98195, USA
[3] Key Laboratory of Space Astronomy and Technology, National Astronomical Observatories, Chinese Academy of Sciences, Beijing 100012, China
[4] Instituto de Astrofísica, Pontificia Universidad Católica de Chile, Av. Vicuña Mackenna 4860, Santiago, Chile
[5] Instituto de Física y Astronomía, Universidad de Valparaíso, Av. Gran Bretaña 1111, Valparaíso, Chile
[6] Centro de Estudios de Fisica del Cosmos de Aragon, Plaza de San Juan 1, Teruel, E-44001, Spain
[7] Instituto de Astrofísica de La Plata (CCT La Plata, CONICET, UNLP), Paseo del Bosque s/n, B1900FWA, La Plata, Argentina
[8] Facultad de Ciencias Astronómicas y Geofísicas, Universidad Nacional de La Plata, Paseo del Bosque s/n, B1900FWA, La Plata, Argentina
[9] Consejo Nacional de Investigaciones Científicas y Técnicas, Av. Rivadavia 1917, C1033AAJ, CABA, Argentina
Received 2016 April 25; revised 2016 June 30; accepted 2016 July 9; published 2016 September 21

ABSTRACT

The Large Synoptic Survey Telescope (LSST) will survey the southern sky from 2022–2032 with unprecedented detail. Since the observing strategy can lead to artifacts in the data, we investigate the effects of telescope-pointing offsets (called dithers) on the *r*-band coadded 5σ depth yielded after the 10-year survey. We analyze this survey depth for several geometric patterns of dithers (e.g., random, hexagonal lattice, spiral) with amplitudes as large as the radius of the LSST field of view, implemented on different timescales (per season, per night, per visit). Our results illustrate that per night and per visit dither assignments are more effective than per season assignments. Also, we find that some dither geometries (e.g., hexagonal lattice) are particularly sensitive to the timescale on which the dithers are implemented, while others like random dithers perform well on all timescales. We then model the propagation of depth variations to artificial fluctuations in galaxy counts, which are a systematic for LSS studies. We calculate the bias in galaxy counts caused by the observing strategy accounting for photometric calibration uncertainties, dust extinction, and magnitude cuts; uncertainties in this bias limit our ability to account for structure induced by the observing strategy. We find that after 10 years of the LSST survey, the best dither strategies lead to uncertainties in this bias that are smaller than the minimum statistical floor for a galaxy catalog as deep as $r < 27.5$. A few of these strategies bring the uncertainties close to the statistical floor for $r < 25.7$ after the first year of survey.

Key words: dark energy – large-scale structure of universe – surveys

1. INTRODUCTION

The Large Synoptic Survey Telescope (LSST) is an upcoming wide-field deep survey, designed to make detailed observations of the southern sky. A telescope with an effective aperture of 6.7 m and a 3.2 Gigapixel camera, LSST will survey about 20,000 deg^2 of the sky in *ugrizy* bands over the course of 10 years, with ∼150 visits in each band to each part of the survey area (Abell et al. 2009). While the survey has various goals, from studying near-Earth objects to transient phenomena, its imaging capabilities are particularly promising for studying dark energy. With its wide-deep observation mode, LSST will probe (1) the shear field from weak gravitational lensing, (2) Baryonic Acoustic Oscillations (BAO) in the galaxy power spectrum and correlation functions, (3) the evolution of the galaxy cluster mass function, (4) SNe Ia and their distance-redshift relationship, and (5) time delays from strong gravitational lenses, providing an opportunity to study dark energy from one data set. The nature of these cosmic probes leads to requirements for the survey observing strategy, understood in terms of cadence, i.e., the frequency of visits in a particular filter, and uniformity, i.e., survey depth across various regions of the sky. For goals that are dependent on spatial correlations, such as BAO and additional large-scale structure (LSS) studies, survey uniformity is of critical importance, while time domain science often depends on high cadence.

The baseline LSST observing strategy tiles the sky with hexagons, each of which inscribes an LSST field of view (FOV; Abell et al. 2009). Given that the FOV is approximately circular, the hexagonal tiling leads to regions between the FOV and the inscribed hexagon that overlap when adjacent fields are observed. Therefore, observations at fixed telescope pointings lead to deeper data in these overlapping regions, decreasing survey uniformity and inducing artificial structure specifically at scales corresponding to the expected BAO signal at $z \sim 1$ (Carroll et al. 2014). While the double-coverage data could be discarded to make the survey uniform, the loss would comprise nearly 17% of LSST data (Carroll et al. 2014), equivalent to 1.5 years of survey time. On the other hand, correction methods have been developed for other surveys (e.g., Ross et al. 2012; Leistedt et al. 2015) to post-process and correct for the systematics in the observed data—such an approach could also work for LSST survey uniformity. Here, however, we address the approach of minimizing eventual survey systematics by designing an optimal observing strategy.

Dithers, i.e., telescope pointing offsets, are helpful for reducing systematics. While LSST plans to implement small dithers to compensate for the finite gaps between the CCDs (e.g., McLean 2008), implementing large dithers on the scale of the FOV appears to offer a solution for LSST survey uniformity, reducing the artificial structure by a factor of 10 as compared to the undithered survey (Carroll et al. 2014). In this

paper, we analyze various dither strategies, varying in both the geometric pattern and the timescale on which the pattern is implemented. We develop a methodology for a quantitative comparison of these strategies and explore their effects on survey depth and BAO systematic uncertainty. We introduce the LSST Operations Simulator (OpSim) and the Metrics Analysis Framework (MAF) in Section 2. Then, in Section 3, we describe the variants of the dithers implemented, followed in Section 4 by a discussion of the impacts of the dither strategies on the coadded depth, as well as artificial fluctuations in galaxy counts. We conclude in Section 5, highlighting that our work illustrates the capability to assess the effectiveness of various dither strategies for LSST science goals.

2. THE LSST OpSim AND MAF

The LSST OpSim simulates 10-year surveys, accounting for realistic factors that affect the final data; these considerations include scheduling of observations, telescope pointing, slewing and downtime, site conditions, etc. (Delgado et al. 2014). More specifically, OpSim output contains realizations of LSST metadata, stamped with sky position, time, and filter (Abell et al. 2009), allowing post-processing of the output to simulate different dither strategies.

As mentioned earlier, LSST OpSim tiles the sky with hexagonal tiles. In order to effectively account for the overlapping regions between the hexagons, we utilize the Hierarchical Equal Area isoLatitude Pixelization (HEALPix) package to uniformly tile the sky with equal area pixels (Górski et al. 2005). HEALPix uses nearly square pixels to tile the sky with a resolution parameter $N_{\rm side}$, leading to a total number of pixels $N_{\rm pixels} = 12N_{\rm side}^2$. In our analysis, we use $N_{\rm side} = 256$, giving a total of 786,432 pixels, and effectively tiling each $3\overset{\circ}{.}5$ FOV with about 190 HEALPix pixels. Here we note that our resolution is fourfold higher than that used in Carroll et al. (2014); this improvement ensures that we do not encounter signal aliasing in the angular scale range we study here.

We carry out our analysis within MAF, designed for the analysis of OpSim output in a manner that facilitates hierarchical building of the analysis tools. MAF consists of various classes, of which the most relevant here are *Metrics*, which contain the algorithms for analyzing each HEALPix pixel, and *Stackers*, which provide the functionality of adding columns to the OpSim database; for details, see Jones et al. (2014). Some of our code has already been incorporated into the MAF pipeline[10], and the rest can be found in the LSST GitHub repository.[11]

3. DITHER STRATEGIES

We consider dither strategies with three different timescales: by season, by night, and by visit. A single visit is a set of two 15 s exposures (Ivezic et al. 2008). Since OpSim output does not have a season assignment for the simulated data, we define seasons separately for each field, starting from zero and incrementing the season number when the field's R.A. is overhead in the middle of the day. This leads to 11 seasons for the 10-year data, and we assign the 0th and the 10th seasons the same dither position.

Since fields are scheduled to be visited at least two times in a given night, followed by a typical revisit time of three days (Ivezic et al. 2008), we implement two approaches for the by-night timescale: (1) FieldPerNight, where a new dither position is assigned to each field independently, and (2) PerNight, where a new position is assigned to all fields. The first approach tracks each field and assigns it a new dither position only if it is observed on a new night, while the second approach assigns a dither position to all the fields every night (regardless of whether a particular field is observed or not). For the by-visit timescale, we only consider FieldPerVisit, and for by-season strategies, we consider PerSeason only.

For the dithers, we implement a few geometrical patterns to probe the effects of dither positions themselves. Since the sky is tiled with hexagons inscribed within the $3\overset{\circ}{.}5$ FOV, we restrict all dither positions to lie within these hexagons. For by-season strategies, given that there are only 10 seasons throughout the LSST run, we pick a geometry that allows us to choose 10 dither positions uniformly across the FOV:

- Pentagons: points alongs two pentagons, one inside an inverted, bigger pentagon.

For by-night and by-visit timescales, we consider four different geometries:

- Hexagonal lattice dithers: 217 points arranged on a hexagonal lattice (Krughoff 2016);
- Random dithers: random points chosen within the hexagon such that every dither position is a new random point;
- Repulsive random dithers: after creating a grid of squares inside the hexagon, squares are randomly chosen without replacement. Every dither position is a random point within a chosen square;
- Fermat spiral dithers: 60 points are chosen from the spiral defined by $r \propto \sqrt{\theta}$, where θ is a multiple of the golden angle $137\overset{\circ}{.}508$ (geometry appears in nature; see Muñoz et al. 2014).

Figure 1 shows these geometries and the possible dither positions. We also considered some other variants. For the by-season timescale, we implemented a PentagonDiamond geometry where the first point is at the center of the FOV, followed by nine points arranged along a diamond circumscribed by a pentagon. We find that PentagonDiamond leads to results similar to Pentagons, and discuss only the latter here. We also considered spiral dithers, where equidistant points are chosen along a spiral centered on the FOV and the number of points and coils can be varied, as well as variants of Fermat spiral, in terms of the number of points and θ as a multiple of $77\overset{\circ}{.}508$ or $177\overset{\circ}{.}508$. Our preliminary analysis shows that these spiral geometries behave similar to the 60-point, golden-angle Fermat spiral described above.

To identify the various strategies, we follow a consistent naming scheme: [Geometry]Dither[Field]Per[Timescale], where the absence of "Field" implies dither assignment to all fields, while its presence implies that each field is tracked and assigned a dither position independent of other fields. For instance, SequentialHexDitherPerNight assigns the new dither position to all fields every night, while SequentialHexDitherFieldPerNight assigns it to a field only when it is observed on a new night.

4. ANALYSIS AND RESULTS

We use OpSim data set `enigma_1189`[12], which includes the wide-fast-deep (WFD) survey region as well as five Deep

[10] https://github.com/lsst/sims_maf
[11] https://github.com/LSST-nonproject/sims_maf_contrib
[12] https://www.lsst.org/scientists/simulations/opsim/opsim-v332-benchmark-surveys

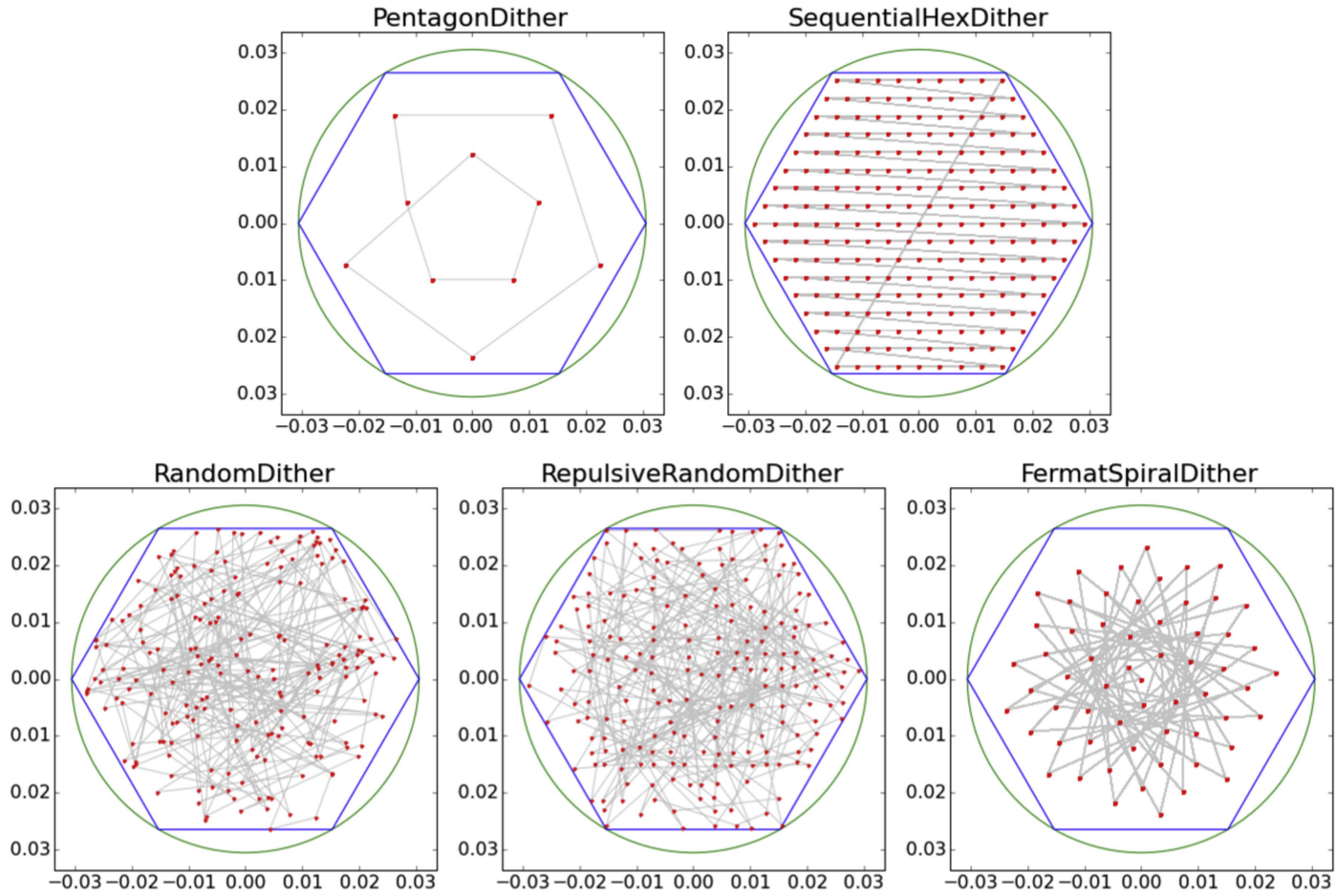

Figure 1. Dither geometries: PentagonDither is implemented only for the per-season timescale, while the rest are implemented for per-visit, per-night and field-per-night timescales. The green curve represents the circular FOV with a radius of 0.305 rad, the blue hexagon represents the hexagonal tiling of the sky originally adopted for the undithered observations, and the red points are the dither positions, connected with gray lines. The axes are labeled in radians. See Section 3 for details.

Drilling fields; we focus only on the WFD survey for our analysis. We implement various dithers within MAF by building *Stackers* corresponding to each dither strategy and post-processing the OpSim output to find the survey results using the dithered positions. First, we examine the *r*-band coadded depth (i.e., the final depth after the 10-year survey) as a function of sky location, followed by an analysis of the fluctuations in the galaxy counts, in order to probe the effects of dither strategies on LSS studies.

4.1. Coadded 5σ Depth

In order to calculate the coadded depth, we use the modified 5σ limiting magnitude data from OpSim, where the limiting magnitude is "modified" in order to represent a real point source detection depth (Ivezic et al. 2008). Assuming that the signal-to-noise ratio adds in quadrature, as it should for optimal weighting of individual images (see, e.g., Gawiser et al. 2006), we calculate the coadded depth, $5\sigma_{\rm stack}$, in each HEALPix pixel from the modified 5σ limiting magnitude summed over individual observations, $5\sigma_{{\rm mod},i}$:

$$5\sigma_{\rm stack} = 1.25\ \log_{10}\left(\sum_i 10^{0.8\times 5\sigma_{{\rm mod},i}}\right). \quad (1)$$

We find that dithered surveys lead to shallower depths near the borders of the survey region, adding significant noise to the corresponding angular power spectra. In order to clean the spectra, we develop a border masking algorithm to discount pixels at the edges of the survey region, comprising nearly 15% of the survey area. See the appendix for details of the masking algorithm.

Figure 2 shows two projections for the *r*-band coadded 5σ depth for the various dither strategies after the shallow border has been masked. The first row shows the Mollweide projection of the coadded depth for NoDither and PentagonDitherPerSeason, while the second row shows the corresponding Cartesian projection, zoomed on the LSST WFD survey area ($-180^\circ <$ R.A. $< 180^\circ$, $-70^\circ <$ decl. $< 10^\circ$). To conserve space, we show only the latter projection for the rest of the dither strategies. We observe that the survey pointings without any dithering lead to deeper overlapping regions between the fields, and consequently a strong honeycomb pattern in the coadded depth. In contrast, the dithered skymaps have comparatively more uniform depth across the survey region, with smaller-scale variations among the dither strategies.

Here we note that although dithering in general weakens the honeycomb pattern seen in the undithered survey, we observe horizontal striping from SequentialHexDitherFieldPerNight; in contrast, SequentialHexDitherPerNight and SequentialHexDitherFieldPerVisit show no such behavior. This is an example where a specific dither strategy's behavior is highly dependent on the timescale on which it is implemented: for PerNight

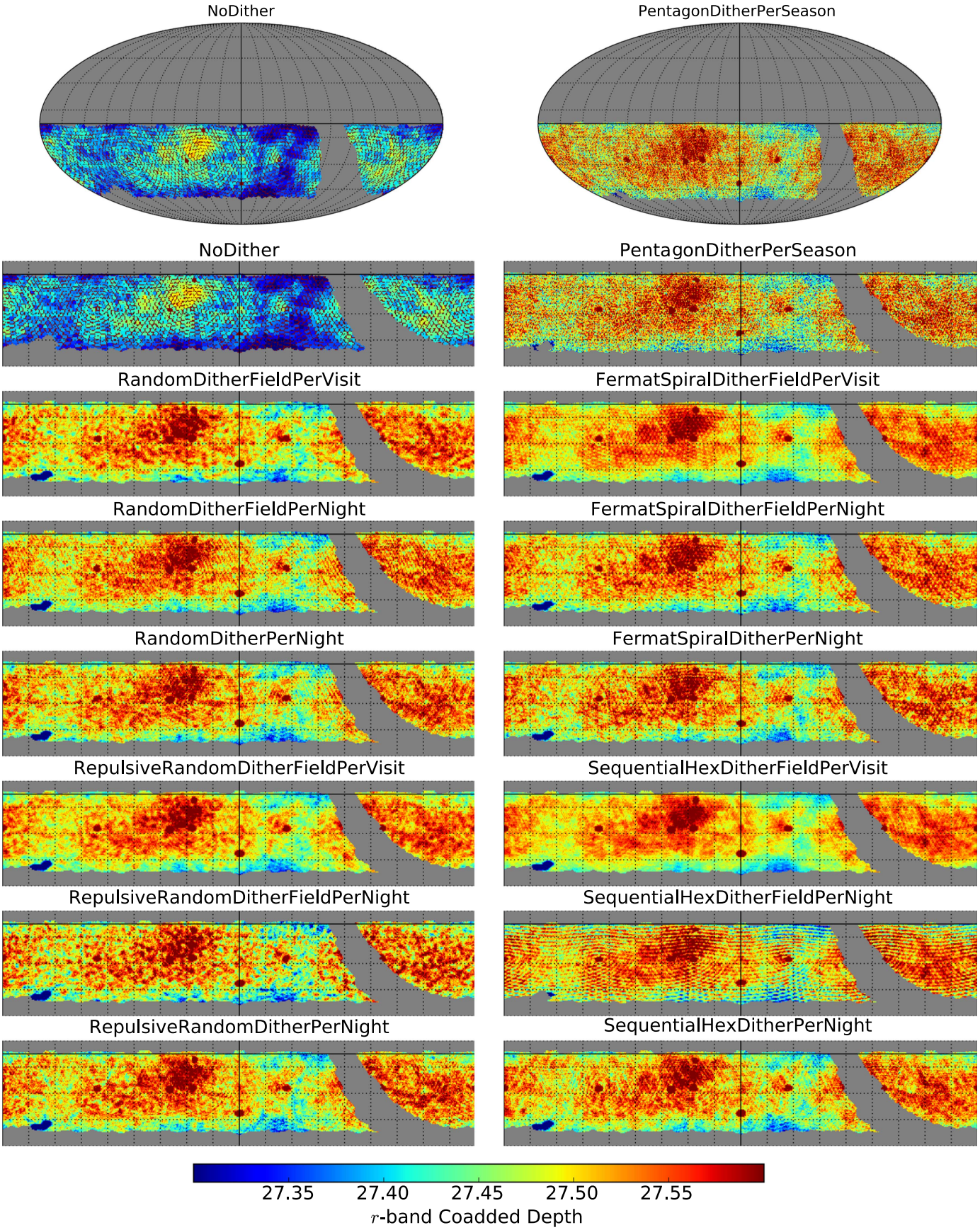

Figure 2. Plots for r-band coadded 5σ depth from various dither strategies, after masking the shallow-depth border. The top row shows the Mollweide projection for two observing strategies, while the second row shows the Cartesian projection restricted to $180^\circ >$ R.A. $> -180^\circ$ (left-right), $-70^\circ <$ Decl. $< 10^\circ$(bottom-top); we only show the latter for the rest of the strategies. We note that the strong honeycomb pattern present in the undithered survey is weaker in the dithered surveys, while for SequentialHexDitherFieldPerNight, we observe strong horizontal striping across the survey region. See Section 4.1 for further details.

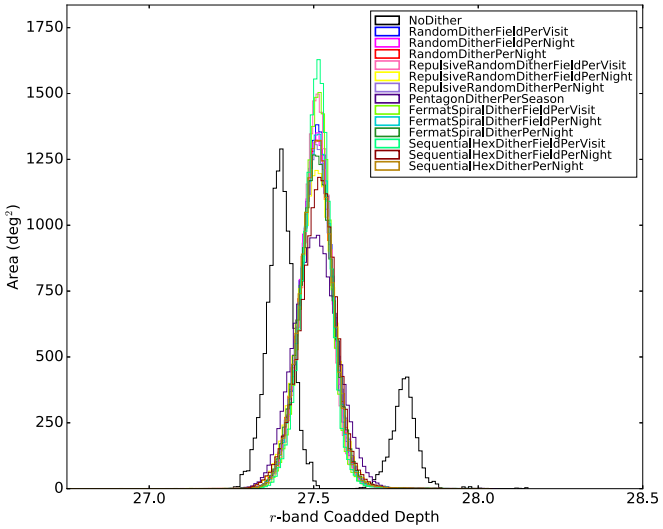

Figure 3. Histogram for the r-band coadded 5σ depth, indicating a bimodal distribution from the undithered survey, and unimodal distributions from the dithered ones.

timescale, a new dither is assigned to all fields every night, implying that the 217-point lattice is traversed multiple times during the ∼3650-night survey. Similarly, for the PerVisit timescale, although a new dither is assigned to each field every time it is visited, the lattice is traversed multiple times given that every field is visited ∼150 times in the r-band throughout the survey. In contrast, for the FieldPerNight timescale, a new dither point is assigned to each field only when it is observed on a new night. Since a given field is only visited on ∼50 nights in a given filter, only the lower part of the lattice is traversed (as the lattice is traversed starting from bottom left), leading to horizontal striping. We verified this conclusion by rotating the hexagonal lattice by 90°, and observing vertical striping for the FieldPerNight timescale.

In Figure 3, we show a histogram of the r-band coadded depth. We see that the undithered survey leads to a bimodal distribution, with the overlapped regions observed much deeper than the rest of the survey. On the other hand, all the dithered surveys lead to unimodal distributions, as dithering leads to observing the data more uniformly, in agreement with Carroll et al. (2014).

In order to quantify the angular characteristics reflected in the skymaps, we measure the power spectrum associated with each of the skymaps. Figure 4 shows the power spectra for the coadded depth from each of the dither strategies considered here; we have removed the monopole and dipole using the HEALPix routine `remove_dipole`. We note that the spectrum corresponding to the undithered survey has a very large peak around $\ell \sim 150$, resulting from the strong honeycomb pattern. In comparison, we see over 10 times less power in the dithered surveys; the $\ell \sim 150$ peak in these surveys is much more comparable to the rest of the spectrum. More specifically, we find that the FieldPerVisit timescale is the most effective at reducing the power for a given dither geometry, while the Random and RepulsiveRandom dithers perform well on all three timescales. Also, we confirm the origins of the $\ell \sim 150$ peak by creating a pure honeycomb, and observing a power spectrum similar to that from the undithered survey.

Furthermore, we see that the horizontal striping in the SequentialHexDitherFieldPerNight skymap generates a large peak around $\ell \sim 150$, while the rest of the dithered spectra do not exhibit such a strong peak. Curiously, the PentagonDitherPerSeason strategy leads to two large peaks around $\ell \sim 270$—a characteristic different from the rest of the dither strategies' but similar to NoDither, with much less power.

To understand the origins of the characteristic patterns in the skymaps, we consider the $a_{\ell \mathrm{m}}$ coefficients of their spherical harmonic transforms. This allows us to produce the skymaps corresponding to specific ranges of the angular scale ℓ. We show our results in Figure 5 for NoDither, PentagonDitherPerSeason, and SequentialHexDitherFieldPerNight strategies. The top row includes the full power spectrum for each strategy, and the second row shows the corresponding Cartesian projection for $0° < \mathrm{R.A.} < 50°$, $-45° < \mathrm{Decl.} < -5°$. The third and fourth rows show the partial skymaps arising from each of the colored peaks shown in the power spectra in the top row. We observe that for the undithered survey, the $\ell \sim 150$ peak arises from the strong honeycomb pattern, while the second peak arises from structure on the small angular scales. For PentagonDitherPerSeason, we see a milder honeycomb for the $\ell \sim 150$ peak, while the $240 < \ell < 300$ peak arises from structure similar to the corresponding one in the undithered survey. Finally, for SequentialHexDitherFieldPerNight, we can see the source of the strong $\ell \sim 150$ peak: the horizontal striping. For higher-ℓ peaks, we note the weaker structure as compared to the other two strategies. We also performed this $a_{\ell \mathrm{m}}$ analysis individually for the two peaks in $240 < \ell < 300$ and found the underlying structures to be very similar.

4.2. Artificial Galaxy Fluctuations

Given our knowledge of the characteristics induced in the coadded depth due to the observing strategy (OS), we now consider the effects of these artifacts on BAO studies. We model the artificial fluctuations in galaxy counts, accounting for photometric calibration errors, dust extinction, and galaxy catalog magnitude cuts. Since BAO studies are redshift dependent, we consider five redshift bins: $0.15 < z < 0.37$, $0.37 < z < 0.66$, $0.66 < z < 1.0$, $1.0 < z < 1.5$, and $1.5 < z < 2.0$.

We first estimate the number of galaxies in specific redshift bins detected in each pixel at a particular depth using a mock LSST catalog, which is constructed using the outputs of the SAG semi-analytic model for galaxy formation (Cora 2006; Lagos et al. 2008; Tecce et al. 2010; Orsi et al. 2014; Gargiulo et al. 2015; Muñoz Arancibia et al. 2015). The model incorporates differential equations for gas cooling, quiescent star formation, energetic and chemical supernova feedback, the growth of a supermassive black hole, the associated AGN feedback, bursty star formation in mergers, and disk instabilities, all coupled to the merger trees extracted from a dark matter simulation run with GADGET2 (Springel 2005), assuming the standard ΛCDM model (Jarosik et al. 2011). The subhalo populations of merger trees are found using SUBFIND (Springel et al. 2001) after the DM halos were identified using a friends-of-friends algorithm.

We normalize the total r-band galaxy counts to the empirical cumulative galaxy count estimates for LSST (see Abell

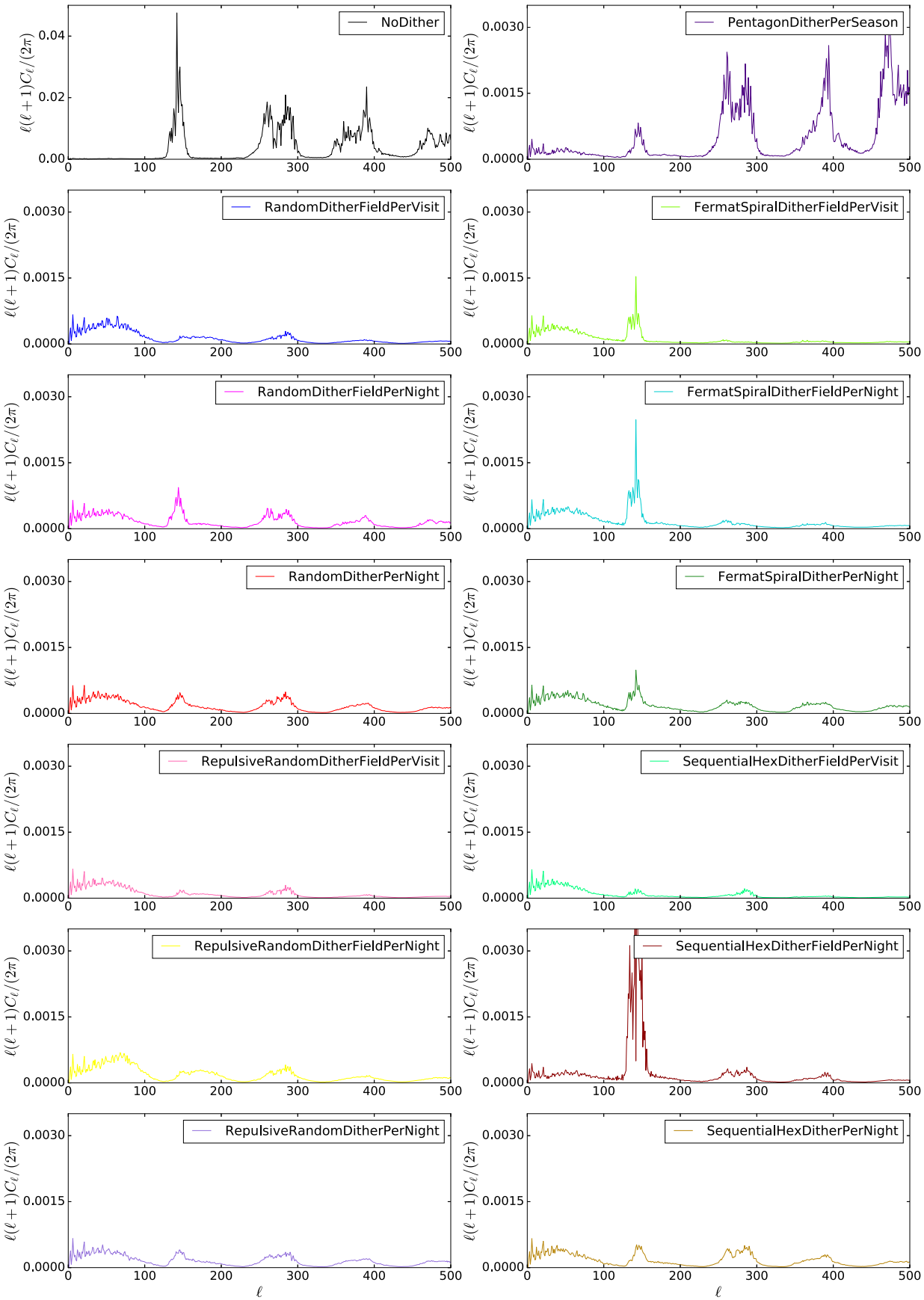

Figure 4. Angular power spectra for the *r*-band coadded depth for all the dither strategies. We note that dithering reduces the angular power by at least a factor of 10 as compared to NoDither. The honeycomb pattern in the undithered survey generates a large peak around $\ell \sim 150$, while dithering of all kinds decreases the spurious power. The horizontal striping in SequentialHexDitherFieldPerNight also creates a moderate peak around $\ell \sim 150$.

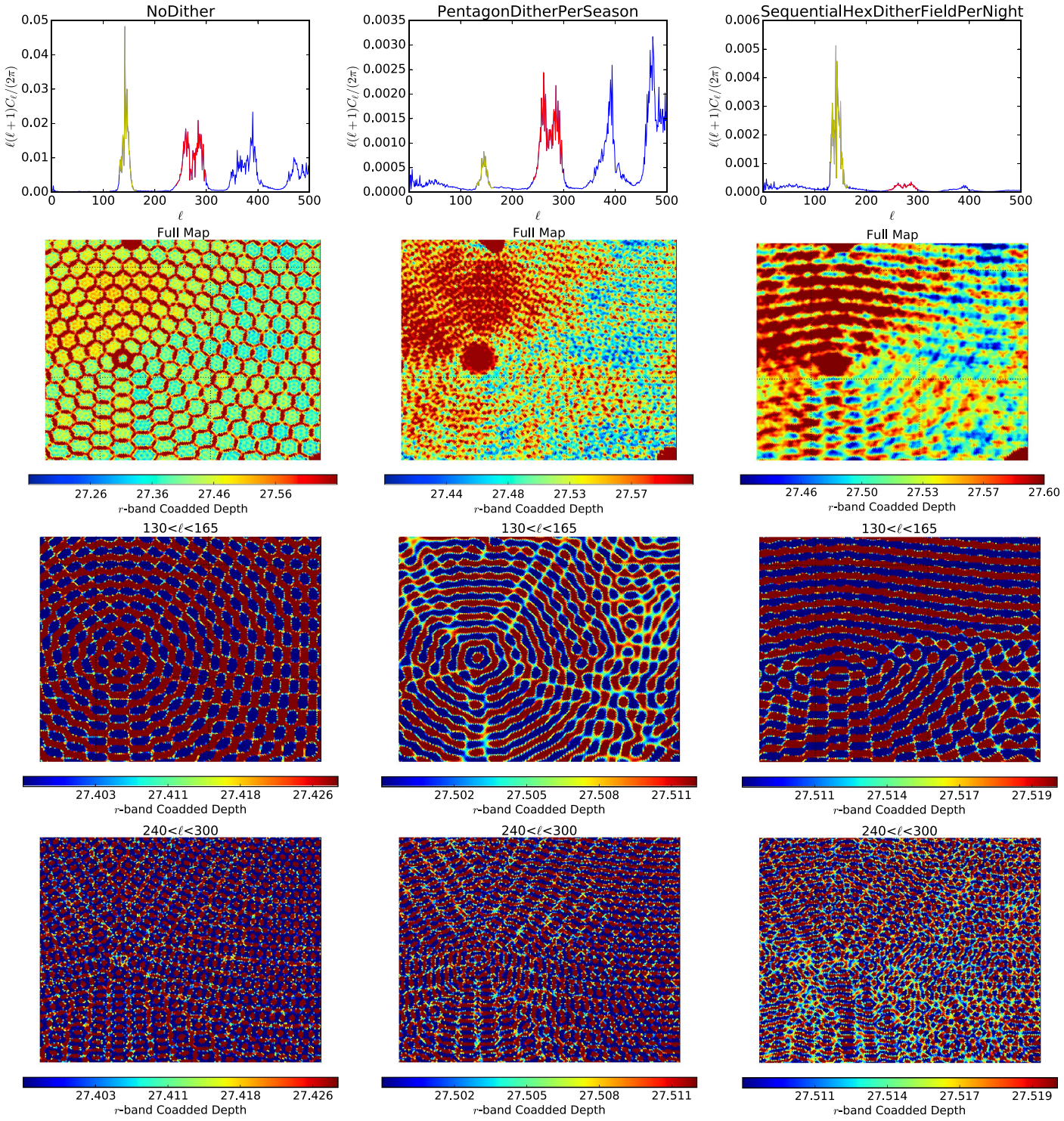

Figure 5. $a_{\ell m}$ analysis plots for two ℓ-ranges in the r-band coadded depth power spectra (colored peaks in the top row). The first row shows the full power spectrum for three observing strategies; the second row shows the corresponding skymaps for $50^\circ >$ R.A. $> 0^\circ$ (left-right), $-45^\circ <$ Decl. $< -5^\circ$ (bottom-top). The third row is for $130 < \ell < 165$ (yellow in the power spectra in the first row), and the fourth is for $240 < \ell < 300$ (red in the top row), all in the same R.A., decl. range as the second row. The leftmost column corresponds to NoDither, the middle one corresponds to PentagonDitherPerSeason, and the right one corresponds to SequentialHexDitherFieldPerNight. We see that the honeycomb pattern in the undithered survey and the horizontal striping in SequentialHex generates the $\ell \sim 150$ peak. Also, we see one (partial) Deep Drilling Field at the top, and a pentagonal tile at decl. $= -30^\circ$ resulting from the tiling of the sphere, both of which are smeared out by dithering.

et al. 2009, Section 3.7.2 for details) at a magnitude cut of $r < 25.9$ (corresponding to the CFHTLS Deep survey completeness limit of $i < 25.5$; see Hoekstra et al. 2006; Gwyn 2008 for details). In contrast with Carroll et al. (2014), where Fleming's function (Fleming et al. 1995) was used to account for the incompleteness near the 5σ limit, we use an erfc function. When multiplied by power-law number counts, Fleming's function causes completeness to drop to 20% of its

peak at $r \sim 30$ before rising again, while the erfc incompleteness function correctly damps down for higher magnitudes. We calculate the number of galaxies, $N_{\rm gal}$, in each HEALPix pixel in a given redshift bin as

$$N_{\rm gal} = 0.5 \int_{-\infty}^{m_{\rm max}} {\rm erfc}[a(m - 5\sigma_{\rm stack})] 10^{c_1 m + c_2} dm, \quad (2)$$

where a is the rollover speed and is chosen to be 1, $5\sigma_{\rm stack}$ is the coadded magnitude depth in the given HEALPix pixel, $m_{\rm max}$ is the magnitude cut, and c_1 and c_2 are the power-law constants determined from the mock catalogs for specific redshift bins. Here, we assume galaxies to have average colors, i.e., $u - g = g - r = r - i = 0.4$, and take this into account by modifying c_2 and $m_{\rm max}$ in Equation (2) for u, g, i versus r. Given the sharp decline of the erfc function at high magnitudes and the consequent decline in the differential galaxy counts, we consider a magnitude limit of $r = 32.0$ as no magnitude limit.

Using the number of galaxies in each pixel, we calculate the fluctuations in the galaxy counts $\Delta N/\overline{N}$ as $(N_{\rm gal}/N_{\rm avg}) - 1$, where $N_{\rm avg}$ is the average number of galaxies per pixel across the survey area. Within MAF, this procedure amounts to using a metric to calculate the number of galaxies and then post-processing the galaxy counts to find $\Delta N/\overline{N}$.

Here we note that artificial fluctuations in galaxy counts induced by the observing strategy scale the fluctuations arising due to actual LSS. In our calculations, we assume that LSS affects the local normalization of the galaxy luminosity function in a given redshift bin, not its shape. This assumption is valid as long as LSS does not alter the shape of the faint end of the luminosity function, which dominates the galaxy number counts. More precisely, in the ith pixel,

$$\left(\frac{N_{\rm gal}}{N_{\rm avg}}\right)_{{\rm observed},i} = \left(\frac{N_{\rm gal}}{N_{\rm avg}}\right)_{{\rm OS},i} \left(\frac{N_{\rm gal}}{N_{\rm avg}}\right)_{{\rm LSS},i}. \quad (3)$$

Defining $\delta_i = \Delta N_i/\overline{N} = (N_{{\rm gal},i}/N_{\rm avg}) - 1$, we have

$$(1 + \delta_{{\rm observed},i}) = (1 + \delta_{{\rm OS},i})(1 + \delta_{{\rm LSS},i}). \quad (4)$$

Since the ensemble average of LSS is zero, we have

$$\begin{aligned} \langle \delta_{{\rm observed},i} \rangle &= \langle \delta_{{\rm OS},i} \rangle + \langle \delta_{{\rm LSS},i} \rangle + \langle \delta_{{\rm OS},i} \delta_{{\rm LSS},i} \rangle \\ &= \delta_{{\rm OS},i} + \langle \delta_{{\rm OS},i} \delta_{{\rm LSS},i} \rangle \end{aligned} \quad (5)$$

where the angular brackets $\langle .. \rangle$ indicate an ensemble average, defined as an average over many realizations of the universe with one LSST survey. Hence, we have $\langle \delta_{{\rm OS},i} \rangle = \delta_{{\rm OS},i}$, as the OS-induced structure represents a fixed pattern on the sky for a given LSST observing strategy and OpSim run. Since there is generally no correlation between the OS-induced structure and LSS, the cross-term $\langle \delta_{{\rm OS},i} \delta_{{\rm LSS},i} \rangle$ should be negligible; we check and confirm this for a typical dither pattern. Also, we note that this assumption about the correlation between OS-induced structure and LSS breaks down if the survey strategy is correlated with LSS, e.g., Deep Drilling Fields focused on galaxy clusters, as then $\langle \delta_{{\rm OS},i} \delta_{{\rm LSS},i} \rangle \neq 0$.

Using Equations (4)–(5), we calculate the power in $\delta_{{\rm observed},i}$:

$$\begin{aligned} \langle \delta^2_{{\rm observed},i} \rangle = &\langle \delta^2_{{\rm OS},i} \rangle + \langle \delta^2_{{\rm LSS},i} \rangle \\ &+ 2\langle \delta_{{\rm OS},i} \delta_{{\rm LSS},i} \rangle + 2\langle \delta^2_{{\rm OS},i} \delta_{{\rm LSS},i} \rangle \\ &+ 2\langle \delta_{{\rm OS},i} \delta^2_{{\rm LSS},i} \rangle + \langle \delta^2_{{\rm OS},i} \delta^2_{{\rm LSS},i} \rangle. \end{aligned} \quad (6)$$

As mentioned earlier, $\langle \delta_{{\rm OS},i} \delta_{{\rm LSS},i} \rangle$ is negligible since OS-induced structure and LSS are generally not correlated . To check how higher order terms like $\langle \delta^2_{{\rm OS},i} \delta^2_{{\rm LSS},i} \rangle$ compare with $\langle \delta_{{\rm OS},i} \delta_{{\rm LSS},i} \rangle$, we calculate the cross-spectra for a typical dither pattern. We find that $\langle \delta_{{\rm OS},i} \delta_{{\rm LSS},i} \rangle$ is dominant over $\langle \delta^2_{{\rm OS},i} \delta^2_{{\rm LSS},i} \rangle$ and therefore these higher order terms are also negligible. Therefore,

$$\langle \delta^2_{{\rm observed},i} \rangle \approx \langle \delta^2_{{\rm OS},i} \rangle + \langle \delta^2_{{\rm LSS},i} \rangle = \delta^2_{{\rm OS},i} + \langle \delta^2_{{\rm LSS},i} \rangle, \quad (7)$$

implying that the OS and LSS contribute independently to the observed power. $\delta^2_{{\rm OS},i}$ thus represents a bias in our measurement of LSS.

To consider realistic behavior for the observing strategies, we account for the uncertainties arising from photometric calibrations. Given that related systematic errors correlate with seeing (Leistedt et al. 2015) and are expected to decrease with the number of observations, we model the calibration uncertainty Δ_i in the ith HEALPix pixel as

$$\Delta_i = \frac{k \Delta s_i}{\sqrt{N_{{\rm obs},i}}} \quad (8)$$

where Δs_i is the difference between the average seeing in the ith HEALPix pixel and the average seeing across the map, $N_{{\rm obs},i}$ is the number of observations in the ith pixel, and k is a constant such that the variance $\sigma^2_{\Delta_i} = 0.01^2$, ensuring the expected 1% errors in photometric calibration (Abell et al. 2009). Figure 6 shows skymaps for these simulated uncertainties for example dither strategies. We note that while dithering does not alter the amplitudes of the photometric calibration uncertainties in our model, it helps mitigate the sharp hexagonal pattern seen in the uncertainties in the undithered survey.

In order to account for the fluctuations in the galaxy counts arising due to the photometric calibration uncertainties, we modify the upper limit on the magnitude in Equation (2) to be $m_{\rm max} + \Delta_i$ for the ith pixel. Since the calibration uncertainties are small, the skymaps for the fluctuations in the galaxy counts after accounting for the calibration uncertainties are indistinguishable from those without. These are shown in the top row in Figure 7.

Furthermore, we include dust extinction by using the Schlegel-Finkbeiner-Davis dust map (Schlegel et al. 1998) when calculating the coadded depth as well as Poisson noise in the galaxy counts after accounting for both dust extinction and photometric calibration . The bottom row in Figure 7 shows the skymaps for the artificial fluctuations for $0.66 < z < 1.0$ after accounting for photometric calibration uncertainties, dust extinction, and the Poisson noise. We find that dust extinction dominates both photometric calibration uncertainties and Poisson noise; it induces power on large angular scales, but it does not wash out the honeycomb pattern in the undithered survey or its low-level residual in the dithered surveys. These trends remain consistent across the five redshift bins.

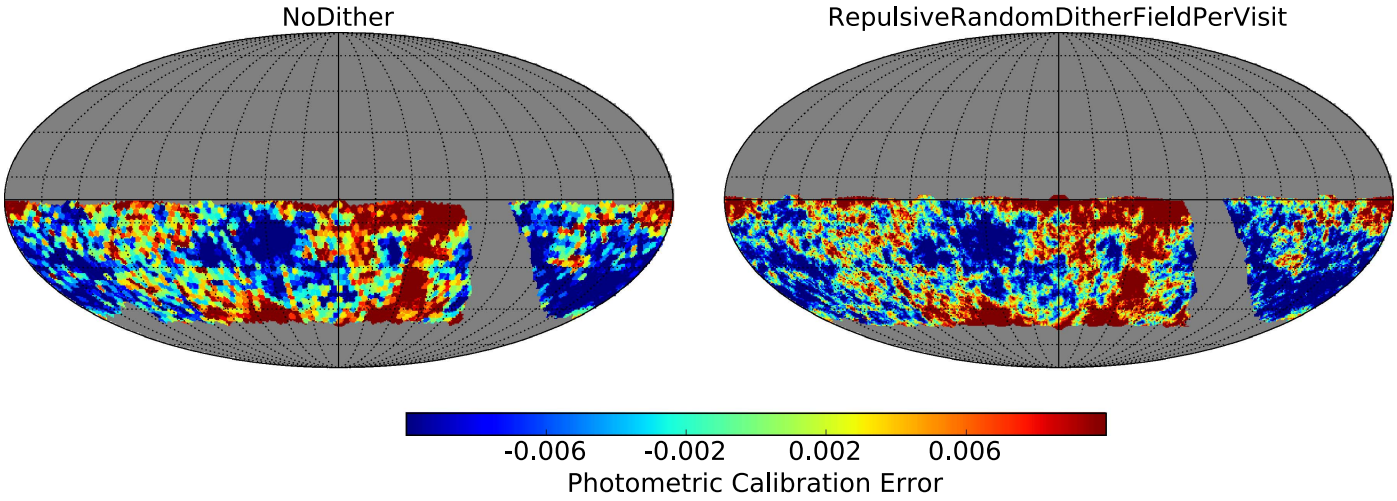

Figure 6. Skymaps of simulated photometric calibration uncertainties for example dither strategies.

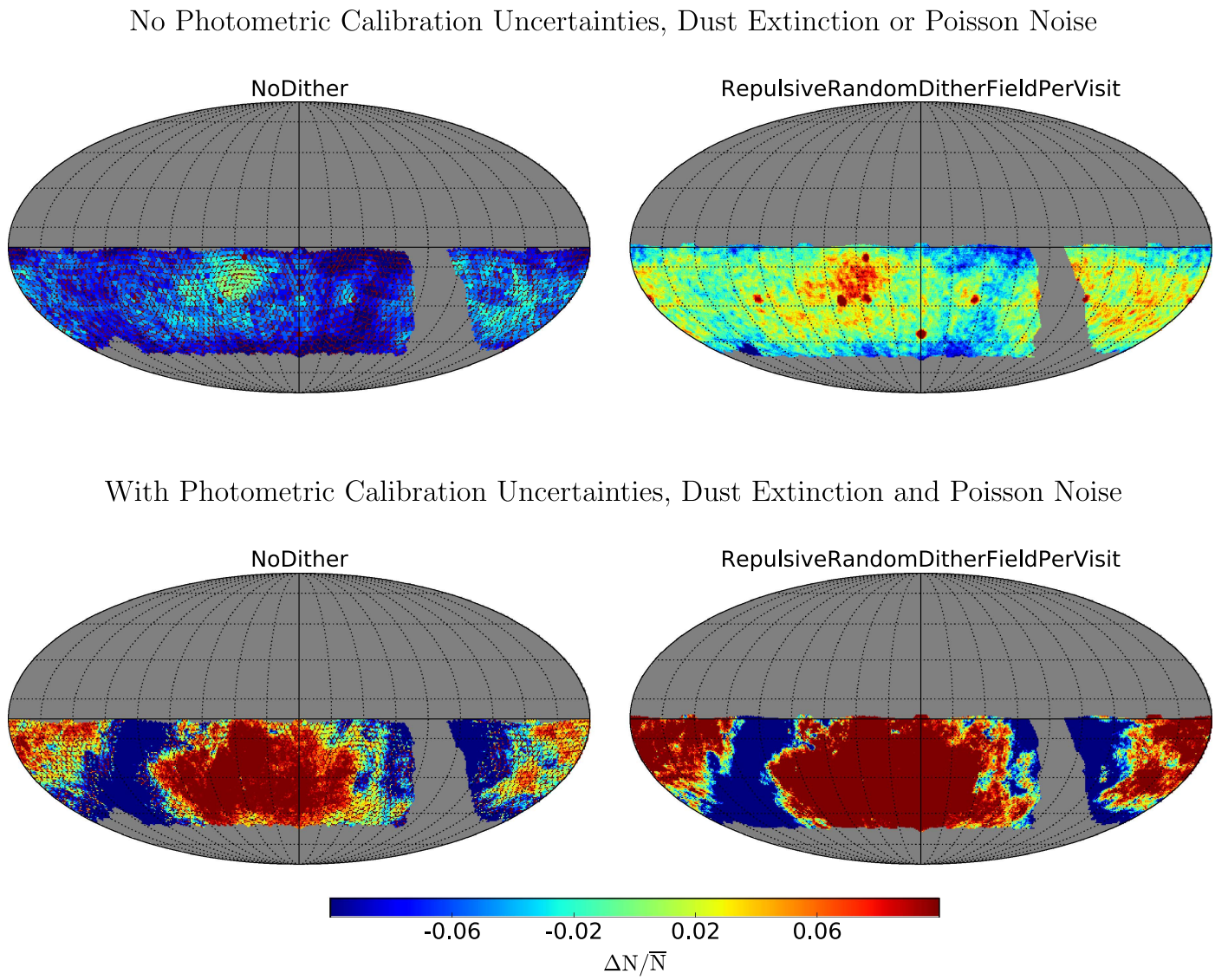

Figure 7. Skymaps for artificial galaxy fluctuations for example dither strategies for $0.66 < z < 1.0$. Top row: without calibration errors, dust extinction, or Poisson noise. Bottom row: after including calibration uncertainties, dust extinction, and Poisson noise. We do not see significant differences in the fluctuations after including the photometric calibration uncertainties or Poisson noise; the skymaps match those in the top row. However, we see that dust extinction dominates the structure on large angular scales. These trends remain consistent across all five z-bins.

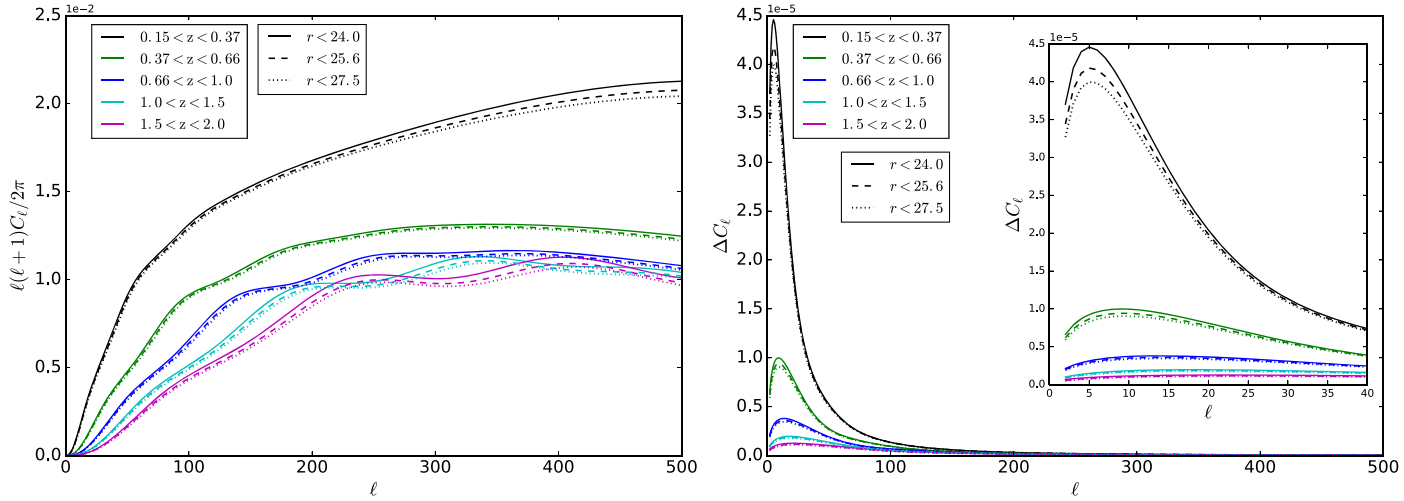

Figure 8. Left: simulated full-sky, pixelized galaxy power spectra with BAO signal from five different redshift bins for three galaxy catalogs: $r < 24.0$, 25.6, 27.5. Right: minimum statistical error associated with measuring the signal in the left panel, with lower-ℓ range shown in the inset. We observe that neither curve changes significantly with magnitude cuts considered in Section 4.2.

Finally, in order to account for the spurious power introduced by the depth variations, we consider the relationship between the measured power spectrum and the true one, for a perfectly uniform survey:

$$\langle P_{\rm measured}(\boldsymbol{k})\rangle = \int d\boldsymbol{k}'\, P_{\rm true}(k')\, |W(\boldsymbol{k}-\boldsymbol{k}')|^2, \quad (9)$$

where $W(\boldsymbol{k}-\boldsymbol{k}')$ is the survey window function, accounting for the effective survey geometry (Feldman et al. 1994; Sato et al. 2013). Projecting the 3D $\boldsymbol{k}$-space onto the 2D ℓ-space, we have

$$C_{\ell,\rm measured} = \sum_{\ell'} |W_{\ell-\ell'}|^2 \langle C_{\ell'}\rangle + \delta C_\ell, \quad (10)$$

where $\langle C_\ell\rangle$ is the expected power spectrum on the full sky, and δC_ℓ is an error term whose minimum variance is given by (see Dodelson 2003, Chapter 8 for details)

$$(\Delta C_\ell)^2 = \frac{2}{f_{\rm sky}(2\ell+1)}\langle C_\ell\rangle^2, \quad (11)$$

where $f_{\rm sky}$ is the fraction of the sky observed, accounting for the reduction in observed power due to incomplete sky coverage. Since we consider only the WFD survey with masked shallow borders, $f_{\rm sky} \approx 37\%$–39% for the dithered surveys, while $f_{\rm sky} \approx 36\%$ for the undithered survey. The expected power spectrum can be defined as

$$\langle C_\ell\rangle = C_{\ell,\rm LSS} + \frac{1}{\overline{\eta}}, \quad (12)$$

where $\overline{\eta}$ is the surface number density in steradians^{-1}; see Fall (1978), Huterer et al. (2001), and Jing (2005) for details. The first term in Equation (12) is the LSS contribution to the expected power spectrum, while the second term is the shot noise contribution arising from discrete signal sampling.

With no LSS and negligible shot noise, $\langle C_\ell\rangle \to 0$. However, as shown in Equation (7) , the observing strategy induces a bias in the measured power spectrum, leading to non-zero power even when $\langle C_\ell\rangle \to 0$. The uncertainty in this bias caused by imperfect knowledge of the survey performance limits our ability to correct for the OS-induced artificial structure. More quantitatively, we have

$$(\sigma_{C_{\ell,\rm measured}})^2 = (\Delta C_\ell)^2 + (\sigma_{C_{\ell,\rm OS}})^2, \quad (13)$$

where the first term on the right is the minimum statistical uncertainty defined in Equation (11), while the second term corresponds to the contribution from the uncertainty in the bias induced by the observing strategy. Since the "statistical floor" ΔC_ℓ assumes no bias in C_ℓ measurements caused by the observing strategy, the OS-induced uncertainty $\sigma_{C_{\ell,\rm OS}}$ must be subdominant to the statistical floor for an optimal measurement of BAO at a given redshift, i.e.,

$$\sigma_{C_{\ell,\rm OS}} \ll \Delta C_\ell = \sqrt{\frac{2}{f_{\rm sky}(2\ell+1)}}\left(C_{\ell,\rm LSS} + \frac{1}{\overline{\eta}}\right). \quad (14)$$

Here we note that the right side in Equation (14) is formally derived in Shafer & Huterer (2015); also see Huterer et al. (2013). These papers offer a detailed theoretical treatment of artificial structure induced by calibration errors, and while our approach is similar to theirs, we incorporate the additional effects of dust extinction, variations in survey depth, and incompleteness in galaxy detection.

Considering the case where $C_{\ell,\rm LSS} = 0$, we find $C_{\ell,\rm measured}$, giving us $C_{\ell,\rm OS}$ for each band and magnitude cut. Since *ugri* bands are the deepest and appear to have the greatest influence on photometric redshifts (A. Prakash 2016, private communication), we model the overall bias as the mean $C_{\ell,\rm OS}$ across the four bands. We calculate $\sigma_{C_{\ell,\rm OS}}$ as the standard deviation of $C_{\ell,\rm OS}$ across the *ugri* bands, modeling uncertainties due to detecting galaxy catalogs in different bands. Therefore, $\sigma_{C_{\ell,\rm OS}}$ should provide a conservative upper limit on the true uncertainty in $C_{\ell,\rm OS}$.

The left panel in Figure 8 shows the full-sky galaxy power spectrum with the BAO signal for three galaxy catalogs, $r < 24.0$, 25.6, 27.5, for the five redshift bins: $0.15 < z < 0.37$, $0.37 < z < 0.66$, $0.66 < z < 1.0$, $1.0 < z < 1.5$, and $1.5 < z < 2.0$. These spectra are pixelized in order to account for the finite angular resolution of our survey simulations, especially when comparing the uncertainties in $C_{\ell,\rm OS}$ with the minimum statistical

Table 1
Estimated Number of Galaxies from *r*-band Coadded Depth after the 10-year Survey for $0.15 < z < 2.0$, after Accounting for Photometric Calibration Errors, Dust Extinction, and Poisson Noise

	$r < 27.5$	$r < 25.7$	$r < 24.0$
Number of Galaxies from NoDither	1.0×10^{10}	4.3×10^{9}	1.6×10^{9}
Percent Improvements in Comparison with NoDither:			
PentagonDitherPerSeason	7.0	6.6	6.6
SequentialHexDitherFieldPerVisit	8.1	7.8	7.9
SequentialHexDitherFieldPerNight	4.9	4.3	4.4
SequentialHexDitherPerNight	8.3	8.0	8.1
FermatSpiralDitherFieldPerVisit	7.6	7.2	7.3
FermatSpiralDitherFieldPerNight	7.6	7.2	7.3
FermatSpiralDitherPerNight	7.4	7.0	7.1
RandomDitherFieldPerVisit	8.7	8.4	8.5
RandomDitherFieldPerNight	8.3	8.0	8.1
RandomDitherPerNight	8.5	8.2	8.3
RepulsiveRandomDitherFieldPerVisit	8.9	8.5	8.7
RepulsiveRandomDitherFieldPerNight	8.6	8.4	8.5
RepulsiveRandomDitherPerNight	8.3	7.9	8.0

Note. We observe a 6.5%–9% improvement in the estimated number of galaxies from dithered surveys in comparison with the undithered survey, across the three magnitude cuts. The exception is SequentialHexDitherFieldPerNight, where the improvement is only 4%–5%.

error in measuring BAO. Assuming that all the HEALPix pixels are identical, the pixelized power spectra can be approximated by multiplying the galaxy power spectra with the pixel window function.[13]

The galaxy power spectra are calculated using the code from Zhan (2006), with modifications to account for BAO signal damping due to nonlinear evolution (Eisenstein et al. 2007). Using the galaxy redshift distribution from Abell et al. (2009), galaxies are assigned to the five redshift bins according to their photometric redshifts, with a time-varying but scale-independent galaxy bias of $b(z) = 1 + 0.84z$ over scales of interest and a simple photometric redshift error model, $\sigma_z = 0.05(1 + z)$. Here we assume the cosmology with $w_0 = -1$, $w_a = 0$, $\Omega_m = 0.127$, $\Omega_b = 0.0223$, $\Omega_k = 0$, spectral index of the primordial scalar perturbation power spectrum $n_s = 0.951$, and primordial curvature power spectrum at $k = 0.05\,\mathrm{Mpc}^{-1}$, $\Delta^2_R = 2 \times 10^{-9}$.

The right panel in Figure 8 shows the minimum statistical uncertainty for the five redshift bins for all three galaxy catalogs; the uncertainties are calculated using $f_{\rm sky}$ from the undithered survey. We observe that while shallower galaxy catalogs lead to larger C_ℓ and ΔC_ℓ, the difference is small and decreases with increasing redshift. For the lowest z-bin, $0.15 < z < 0.37$, there is only about an 8% increase in C_ℓ and ΔC_ℓ when comparing the $r < 25.6$ catalog with $r < 24.0$.

First we calculate $C_{\ell,\rm OS}$ and its uncertainties for $0.66 < z < 1.0$ after only one year of survey in order to explore the quality of BAO study the first data release will allow. Figure 9 shows the $C_{\ell,\rm OS}$ uncertainties as well as the minimum statistical error for $0.66 < z < 1.0$ for various observing strategies, for $r < 24.0$ and $r < 25.7$ (corresponding to the gold sample, $i < 25.3$). We observe that the undithered survey leads to $C_{\ell,\rm OS}$ uncertainties that are 1–3× the minimum statistical uncertainty for the gold sample at $\ell > 100$, and only a few dither strategies are effective at reducing the difference. In particular, Random and RepulsiveRandom dithers are the most effective, reducing $\sigma_{C_{\ell,\rm OS}}$ to nearly 1–2× the statistical floor. We note that FermatSpiral and SequentialHex dithers perform nearly as poorly as NoDither when implemented on FieldPerVisit and FieldPerNight timescales, while the PerNight timescale is more effective. On the other hand, we see that FieldPerVisit and FieldPerNight lead to smaller uncertainties for Random and RepulsiveRandom geometries. As expected, we see that a shallower sample $r < 24.0$ reduces the $C_{\ell,\rm OS}$ uncertainties; the undithered survey still leads to $\sigma_{C_{\ell,\rm OS}}$ about 3× the statistical floor, while Random and RepulsiveRandom dithers lead to uncertainties comparable to the statistical floor on some timescales. Here we note that since we do not mask borders when considering the one-year data, $f_{\rm sky} \approx 42\%$–45% for the one-year survey, depending on the dither strategy.

We then extend the calculation of the OS-induced power to the full 10-year survey. Figure 10 shows $\sigma_{C_{\ell,\rm OS}}$ as well as ΔC_ℓ for $0.66 < z < 1.0$ for three different magnitude cuts: $r < 24.0$, $r < 25.7$ and $r < 27.5$. We find that the undithered survey leads to $\sigma_{C_{\ell,\rm OS}}$ 0.2–4 times the minimum statistical floor for $r < 25.7$ and $r < 27.5$; at $\ell > 100$, only a very strict cut of $r < 24.0$ brings $\sigma_{C_{\ell,\rm OS}}$ below ΔC_ℓ. However, most dither strategies reduce the uncertainties below the statistical floor for galaxy catalogs as deep as $r < 27.5$, with exceptions of SequentialHex dithers on FieldPerVisit and FieldPerNight timescales. We note here that systematics correction methods such as template subtraction and mode projection can be applied to further reduce the contribution of $C_{\ell,\rm OS}$ to the total C_ℓ uncertainties; e.g., see Elsner et al. (2016), Holmes et al. (2012). Such application appears necessary for the one-year survey as optimizing the observing strategy alone does not reduce the uncertainties in $C_{\ell,\rm OS}$ below ΔC_ℓ. However, the correction methods may not lead to significant improvements for a dithered 10-year survey, as optimizing the observing strategy is effective in reducing the uncertainties in $C_{\ell,\rm OS}$ well below the statistical floor.

[13] See Appendix B in the HEALPix primer: http://healpix.sourceforge.net/pdf/intro.pdf.

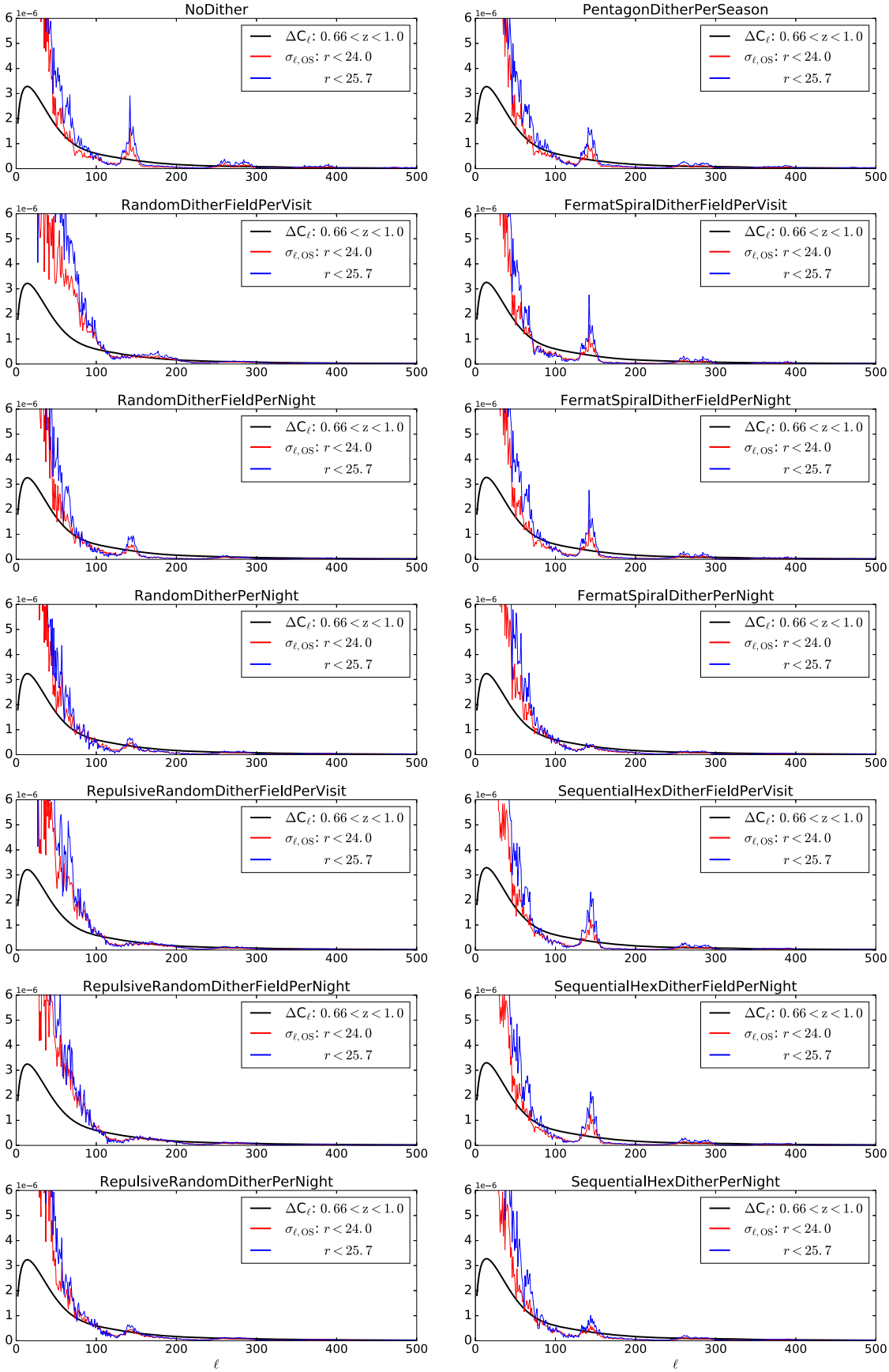

Figure 9. Comparison of the uncertainty in the OS-induced bias $\sigma_{\ell,\mathrm{OS}}$ with the minimum statistical uncertainty ΔC_ℓ for $0.66 < z < 1.0$ for different magnitude cuts after only one year of survey.

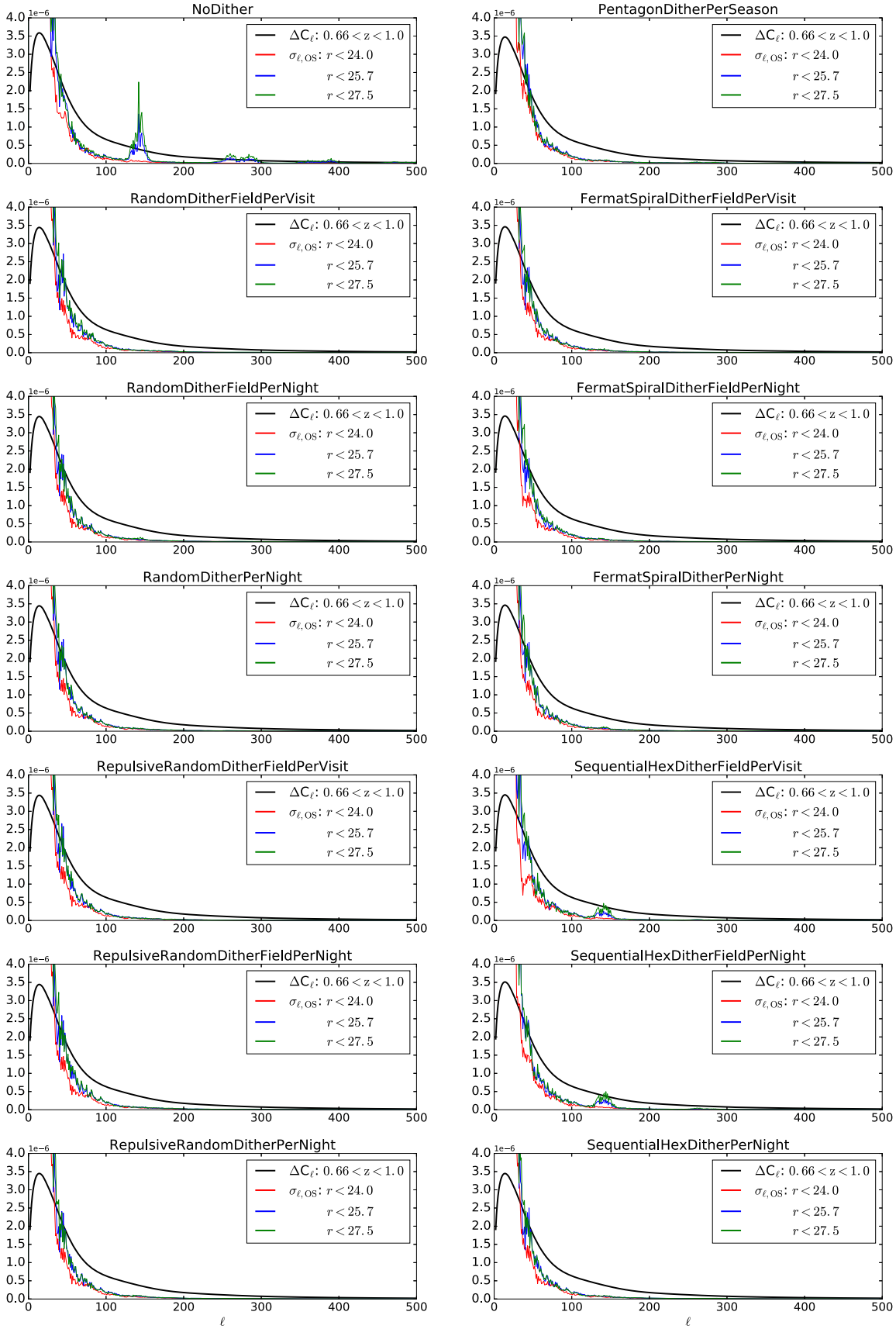

Figure 10. Comparison of the uncertainty in the OS-induced bias $\sigma_{\ell,\mathrm{OS}}$ with the minimum statistical uncertainty ΔC_ℓ for $0.66 < z < 1.0$ for different magnitude cuts after the full 10-year survey.

To further our understanding, we repeat the 1-year and 10-year analysis for $1.5 < z < 2.0$. We find similar qualitative results as those from $0.66 < z < 1.0$ analysis: for the 1-year survey, Random and RepulsiveRandom perform well alongside FermatSpiral and SequentialHex on the PerNight timescale, while most dither strategies are effective for the 10-year survey, with the exception of SequentialHex on FieldPerVisit and FieldPerNight timescales.

The effect of magnitude cuts is further illustrated in Table 1, which includes the estimated number of galaxies for $0.15 < z < 2.0$ from the r-band coadded depth for the 10-year survey after accounting for photometric calibration errors, dust extinction, and Poisson noise. We see that each magnitude cut eliminates a substantial number of galaxies. Also, as in Carroll et al. (2014), we see that dithering increases the estimated number of galaxies when compared to the undithered survey; the fractional difference in the number of galaxies from dithered to undithered surveys decreases with shallower surveys.

5. CONCLUSIONS

It is critical to develop an LSST observing strategy that will maximize the data quality for its science goals. In this work, we analyzed the effects of dither strategies on r-band coadded 5σ depth to study the feasibility of increasing the uniformity across the survey region. We investigated different dither geometries on different timescales, and illustrated how a specific geometrical pattern (e.g., hexagonal lattice) can perform quite differently when implemented on different timescales. We find that per-visit and per-night implementations outperform field-per-night and per-season timescales, while some dither geometries (like repulsive random dithers) consistently lead to less spurious power for all the timescales on which the dither positions are assigned. We also performed an $a_{\ell \mathrm{m}}$ analysis to probe the origins of some of the characteristic patterns induced by the observing strategies. Our work illustrates the sensitivity of depth uniformity to the dither strategy.

We then considered how the artifacts in coadded depth produce fluctuations in galaxy counts; we calculate the uncertainties in the bias induced by the observing strategy, which limits our ability to correct for the spurious structure. We find that after accounting for photometric calibration uncertainties, dust extinction, Poisson noise and reasonable magnitude cuts, dithers of most kinds are effective in reducing the uncertainties in the observing-strategy-induced bias below the minimum statistical uncertainty in the measured galaxy power spectrum. Specifically, we find that RepulsiveRandom dithers implemented on per-visit and field-per-night timescales are the most effective for the $0.66 < z < 1.0$ sample after only one year of survey, although they do not bring down the uncertainties in the induced bias below the minimum statistical floor for $r < 25.7$. As for the full 10-year survey, we find that all dither strategies (except per-visit and field-per-night SequentialHex dithers) bring down the uncertainties below the statistical floor for a galaxy catalog as deep as $r < 27.5$. We find similar results for all redshift bins.

To precisely determine the limiting uncertainties in the bias induced by the observing strategy, more detailed LSST simulations are needed, including photometric redshifts, input LSS, and further systematics reduction methods, e.g., mode projection accounting for imperfect detectors and the consequent instrumental effects. Also, while our work illustrates the impact of dithers on LSS studies, the differences between some dither geometries are small and therefore need more detailed investigation to determine conclusively which is the best dither strategy, alongside an analysis of the impacts of various dither strategies on other science goals. Such analyses will facilitate a more definitive measure of the precision with which LSST data will allow high redshift studies of LSS.

This research was supported by the Department of Energy (grant DE-SC0011636) and the National Science Foundation (REU grant PHY-1263280). Hu Zhan was partially supported by the Chinese Academy of Sciences (grant XDB09000000), and Alejandra M. Muñoz Arancibia was supported by FONDECYT (grant 3160776) and BASAL CATA PFB-06. Nelson D. Padilla also acknowledges support from BASAL CATA PFB-06 and FONDECYT (grant 1150300); the light cones were run using the Geryon cluster hosted at the Centro de Astro-Ingenieria UC. Sofía A. Cora acknowledges support from Consejo Nacional de Investigaciones Científicas y Técnicas, Agencia Nacional de Promoción Científica y Tecnológica, and Universidad Nacional de La Plata, Argentina. We thank K. Simon Krughoff for suggesting the hexagonal dither pattern for LSST, and Abhishek Prakash, Jeff Newman, Andy Connolly, Rachel Mandelbaum, Dragan Huterer, Terry Matilsky, and Seth Digel for helpful comments, conversations, and insights. Finally, we thank the LSST Dark Energy Science Collaboration for feedback on the design and conduct of this research.

APPENDIX
BORDER MASKING ALGORITHM

In Figure 11, we show skymaps (left column) and the corresponding power spectrum (right column) for the r-band coadded 5σ depth from the undithered survey and an example dithered survey. While the dithered survey does not have the strong honeycomb seen in the undithered case, we notice that the border of the dithered survey area is much shallower than the rest of the survey. This variation in depth carries over to the power spectrum as strong oscillations, especially at small ℓ. In order to minimize this effect, we develop a border masking algorithm to mask the pixels within a specific "pixel radius" from the edge of the survey area. For this purpose, we utilize the distinction between out-of-survey and in-survey area in MAF: the former is masked, and the analysis only accounts for the data in the unmasked portion of the data array. Using this distinction and the HEALPix routine `get_all_neighbours`, we find the unmasked pixels with masked neighbors, effectively finding the edge of the survey. We parametrize the number of iterations for this neighbor finding algorithm, and choose the number of iterations (determined by what we call the pixel radius) that removes the shallow border. The masking algorithm can be found on GitHub[14].

Working at $N_{\mathrm{side}} = 256$ resolution, we mask all the pixels within a 14 pixel radius from the edge of survey, effectively masking ~15% of the survey area. The bottom row in Figure 11 shows the dithered skymap and the corresponding power spectrum after the shallow border has been removed. We notice a stark difference between the power spectrum before and after the border masking, as removing the shallow border allows the in-survey variations to be seen much more clearly.

[14] https://github.com/LSST-nonproject/sims_maf_contrib/blob/master/mafContrib/maskingAlgorithmGeneralized.py

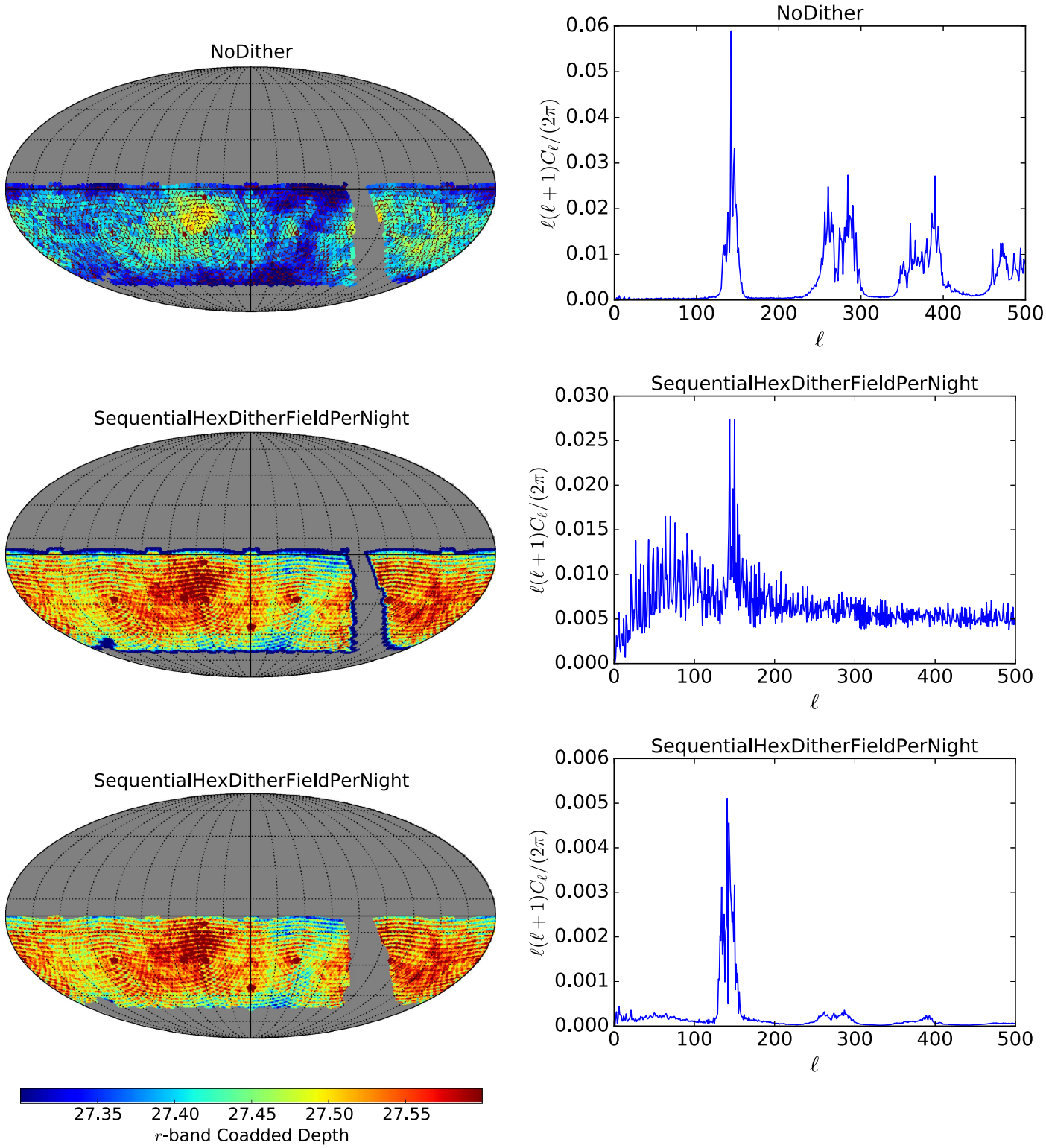

Figure 11. Left column: skymaps for r-band coadded 5σ depth for example dither strategies. Right column: angular power spectra corresponding to the skymaps in the first column. Top and middle rows show the data without any border masking. We note that the undithered survey does not lead to any shallow edges, while the dithered survey does. The shallow-depth edge leads to a noisy power spectrum, shown in the middle right panel. After removing the shallow-border by implementing 14 pixel-radius masking, we see a reduction in the low-ℓ power, and therefore a cleaner spectrum.

REFERENCES

Abell, P. A., Allison, J., Anderson, S. F., et al. 2009, arXiv:0912.0201
Carroll, C. M., Gawiser, E., Kurczynski, P. L., et al. 2014, Proc. SPIE, 9149, 91490C
Cora, S. A. 2006, MNRAS, 368, 1540
Delgado, F., Saha, A., Chandrasekharan, S., et al. 2014, Proc. SPIE, 9150, 15
Dodelson, S. 2003, Modern Cosmology (New York, NY: Academic Press)
Eisenstein, D. J., Seo, H.-J., & White, M. 2007, ApJ, 664, 660
Elsner, F., Leistedt, B., & Peiris, H. V. 2016, MNRAS, 456, 2095
Fall, S. M. 1978, MNRAS, 185, 165
Feldman, H. A., Kaiser, N., & Peacock, J. A. 1994, ApJ, 426, 23
Fleming, D. E. B., Harris, W. E., Pritchet, C. J., & Hanes, D. A. 1995, AJ, 109, 1044
Gargiulo, I. D., Cora, S. A., Padilla, N. D., et al. 2015, MNRAS, 446, 3820
Gawiser, E., van Dokkum, P. G., Herrera, D., et al. 2006, ApJS, 162, 1
Górski, K. M., Hivon, E., Banday, A. J., et al. 2005, ApJ, 622, 759
Gwyn, S. D. J. 2008, PASP, 120, 212
Hoekstra, H., Mellier, Y., van Waerbeke, L., et al. 2006, ApJ, 647, 116
Holmes, R., Hogg, D. W., & Rix, H.-W. 2012, PASP, 124, 1219
Huterer, D., Cunha, C. E., & Fang, W. 2013, MNRAS, 432, 2945
Huterer, D., Knox, L., & Nichol, R. C. 2001, ApJ, 555, 547
Ivezic, Z., Tyson, J., Acosta, E., et al. 2008, arXiv:0805.2366
Jarosik, N., Bennett, C. L., Dunkley, J., et al. 2011, ApJS, 192, 14
Jing, Y. P. 2005, ApJ, 620, 559
Jones, R. L., Yoachim, P., Chandrasekharan, S., et al. 2014, Proc. SPIE, 9149, 91490B
Krughoff, K. 2016, Hexagonal Dithering for LSST, Zenodo, doi:10.5281/zenodo.55701
Lagos, C. D. P., Cora, S. A., & Padilla, N. D. 2008, MNRAS, 388, 587
Leistedt, B., Peiris, H. V., Elsner, F., et al. 2015, arXiv:1507.05647
McLean, I. 2008, Electronic Imaging in Astronomy: Detectors and Instrumentation (Berlin: Springer)
Muñoz Arancibia, A. M., Navarrete, F. P., Padilla, N. D., et al. 2015, MNRAS, 446, 2291
Muñoz, R. P., Puzia, T. H., Lançon, A., et al. 2014, ApJS, 210, 4
Orsi, Á., Padilla, N., Groves, B., et al. 2014, MNRAS, 443, 799
Ross, A. J., Percival, W. J., Sánchez, A. G., et al. 2012, MNRAS, 424, 564
Sato, T., Hütsi, G., Nakamura, G., & Yamamoto, K. 2013, IJAA, 3, 243
Schlegel, D. J., Finkbeiner, D. P., & Davis, M. 1998, ApJ, 500, 525
Shafer, D. L., & Huterer, D. 2015, MNRAS, 447, 2961
Springel, V. 2005, MNRAS, 364, 1105
Springel, V., White, S. D. M., Tormen, G., & Kauffmann, G. 2001, MNRAS, 328, 726
Tecce, T. E., Cora, S. A., Tissera, P. B., Abadi, M. G., & Lagos, C. D. P. 2010, MNRAS, 408, 2008
Zhan, H. 2006, JCAP, 8, 008